Deformation and spallation of shocked Cu bicrystals with Σ3 coherent and symmetric incoherent twin boundaries

W. Z. Han,[1,*] Q. An,[2] S. N. Luo,[1,†] T. C. Germann,[1] D. L. Tonks,[1] and W. A. Goddard III[2]
[1]*Los Alamos National Lab, Los Alamos, New Mexico 87545, USA*
[2]*Materials and Process Simulation Center, California Institute of Technology, Pasadena, California 91125, USA*
(Received 31 October 2011; revised manuscript received 21 December 2011; published 11 January 2012)

We perform molecular dynamics simulations of Cu bicrystals with two important grain boundaries (GBs), Σ3 coherent twin boundaries (CTB), and symmetric incoherent twin boundaries (SITB) under planar shock wave loading. It is revealed that the shock response (deformation and spallation) of the Cu bicrystals strongly depends on the GB characteristics. At the shock compression stage, elastic shock wave can readily trigger GB plasticity at SITB but not at CTB. The SITB can induce considerable wave attenuation such as the elastic precursor decay via activating GB dislocations. For example, our simulations of a Cu multilayer structure with 53 SITBs (∼1.5-μm thick) demonstrate a ∼80% elastic shock decay. At the tension stage, spallation tends to occur at CTB but not at SITB due to the high mobility of SITB. The SITB region transforms into a threefold twin via a sequential partial dislocation slip mechanism, while CTB preserves its integrity before spallation. In addition, deformation twinning is a mechanism for inducing surface step during shock tension stage. The drastically different shock response of CTB and SITB could in principle be exploited for, or benefit, interface engineering and materials design.

DOI: 10.1103/PhysRevB.85.024107 PACS number(s): 61.72.Mm, 62.50.Ef, 61.72.Hh, 62.20.F−

I. INTRODUCTION

The mechanical properties of polycrystalline metals are determined to a large extent by the characteristics of their defects or interfaces.[1] It has been commonly remarked that the study of the behavior of a polycrystalline material is often reduced to exploring those of the interfaces.[1] Grain boundaries (GBs), one of the most important interface structures in polycrystalline materials, impact the bulk properties in many aspects.[1–7]

For the shock response of metals (broadly defined to include deformation and spall damage), it has long been recognized that their microstructure plays a critical role, such as grain size, grain orientation, and GB types, etc.[8,9] Shock experiments[8–18] have been routinely performed on polycrystalline solids along with very limited molecular dynamic (MD) simulations in past few decades.[19–27] Given the vast number of GB types and grain characteristics, it is highly desirable to investigate some elemental processes, such as columnar crystals or bicrystals, so we can gain certain specific insights without being overwhelmed by the complexities of abundant random GBs. In addition, due to the highly transient nature of shock events, it is extremely challenging to acquire the real-time measurements of microstructure responses.[8–18] In contrast, MD simulations are capable of supplying real-time data for understanding dynamic materials physics/mechanics of a wide range of materials/microstructures at atomic scales, including single crystals, nanocrystalline metals, glasses, polymers, and composites.[19–27] For instance, we performed MD shock simulations of [100] columnar nanocrystalline Cu and $\Sigma3(00\bar{1})//(22\bar{1})$ nanolaminates[28,29] and showed that the crystallographic anisotropy and GBs induce strong deviations of shock response from perfect planarity through crosstalk between neighboring constituent crystals, as well as pronounced stress and strain concentrations. Both plasticity and spall damage depend strongly on GB characteristics and loading geometry.

MD shock simulations of GBs are still scarce, and it would be helpful to explore some special but widely existing GBs in order to acquire insights into the general shock response of metals. Recently, $\Sigma3\{111\}$ coherent twin boundaries (CTBs) and $\Sigma3\{112\}$ symmetric incoherent twin boundaries (SITBs) have attracted considerable attention, since they often form during fabrication as growth twins and play a crucial role in the mechanical performance of nanotwinned metals.[30–42] In epitaxial nanotwinned Cu, growth twin lamellae have long CTBs normal to the growth direction and truncated by short SITBs.[31,32,34] The nanotwinned Cu has been shown to exhibit a superior combination of ultrahigh strength, low electrical resistance, good ductility, high thermal stability, and fatigue resistance.[31–40] The unusual mechanical properties of nanotwinned Cu originate from CTBs, which act as strong barriers to slip transfer of single dislocations (thus, enhancing strength), and simultaneously create more local sites for nucleating and accommodating dislocations (thus, elevating ductility and improving work hardening).[31] In contrast, recent investigation reveals that the migration of SITBs can lead to detwinning and is a special mechanism for work softening.[40–42] SITBs can be represented as an array of Shockley partial dislocations on a $\{111\}$ plane.[41–43] The detwinning is accomplished via collective glide of those Shockley partial dislocations.[42] Therefore, CTBs are much stronger than SITBs in terms of the GB strength under usual quasistatic loading conditions. However, how do these GBs respond to dynamic loading such as shock waves? It is highly desirable to explore the shock response of CTBs and SITBs by MD simulations in order to fully exploit some unique properties of those GBs.

In this investigation we choose Cu bicrystals containing a CTB or SITB as the model structures for MD shock simulations. Our simulations reveal rich deformation and damage phenomena different for CTB and SITB, as well as underlying mechanisms. In particular, we investigate the interactions between the elastic and plastic shock waves with

GBs, the damping effect of GBs on the elastic and plastic waves, and the dependence of plasticity and spall damage on GBs characteristics. Furthermore, our results show that SITB can avoid damage via GB movement and plasticity around SITB, and spall damage tends to occur at the CTB while not at SITB. Such dynamic phenomenon is not expected in quasistatic loading conditions.

II. SIMULATION DESIGN AND METHODS

CTB and SITB are located at the low-end (22.2 mJm^{-2}) and high-end (591.9 mJm^{-2}) of the $\Sigma 3$ GB energy spectrum, respectively.[44] These two kinds of GBs are very common and often formed at the same time in low-stacking fault-energy metals during, e.g., epitaxial growth.[31–34] In our simulations the orientations of the grains in the bicrystals containing a CTB or SITB are illustrated in Fig. 1. We define the GB normals as the x-axis, and therefore, the x-axis is along $\langle 111 \rangle$ and $\langle 112 \rangle$ for CTB and SITB bicrystals, respectively. The tilt axis ($\langle 110 \rangle$) is the y-axis, and the z-axis is along $\langle 112 \rangle$ and $\langle 111 \rangle$ for CTB and SITB, respectively. Using the coincidence site lattice method, we first construct the CTB and SITB bicrystals (containing only one GB) with edge lengths of $\sim 120 \times 10 \times 10$ nm ($\sim$1 000 000 atoms; each grain is about 60-nm thick along the x-axis). Single crystal flyer plates are constructed separately with the same orientation and dimensions as Grain I in Fig. 1 for both the CTB and SITB cases ($\sim$500 000 atoms). In addition, we construct a Cu-multilayer structure containing 53 SITBs in order to study the elastic precursor decay; the layer thickness is about 27 nm, and the edge lengths are $\sim 1458 \times 10 \times 10$ nm ($\sim$11 200 000 atoms). The grain orientation is similar to the bicrystal in Fig. 1(b).

The atomic interactions in Cu are described with an accurate embedded-atom-method potential.[45] Our MD simulations use the Institut für Theoretische and Angewandte Physik MD code[46] and Large-Scale Atomic/Molecular Massively Parallel Simulator (LAMMPS).[47] The as-constructed bicrystals are relaxed with the conjugate gradient method, followed by thermalization at the ambient conditions with the constant-pressure-temperature ensemble and three-dimensional periodic boundary conditions. The resulting bicrystals are taken as the targets in our shock wave simulations. The flyer plates are also thermalized at ambient conditions. The respective flyer plate and target configurations are assembled along the x-axis [Fig. 2(a)]. In order to facilitate the formation of plastic waves from the impact plane, we intentionally shift the flyer plate by about half an atomic space along the z-axis, relative to the bicrystal target. We denote the equivalent piston velocity as u_p. The flyer plate and target are assigned initial velocities of $4/3\ u_p$ and $-2/3\ u_p$ along the x-axis, respectively, before impacting each other. Here we explore $u_p = 0.375$, 0.5, and 0.75 km/s. Shock simulations use the microcanonical ensemble. Periodic boundary conditions are applied along the y- and z-axes (not the x-axis) to mimic one-dimensional (1D) strain loading of a bicrystal with a single GB normal to the shock direction. The nonimpact sides of the flyer plate and target are free surfaces. The time step for integrating the equation of motion is 1 fs, and the shock simulation durations are up to 60 ps for flyer plate impact. Such flyer plate impact simulations investigate two drastically different GBs: CTB and SITB. Shock simulations of the Cu-multilayer structure are similar to the flyer plate impact simulations, except that we launch the multilayer structure to impact a rigid wall. Similar simulation details can be found in Refs. 26 and 27.

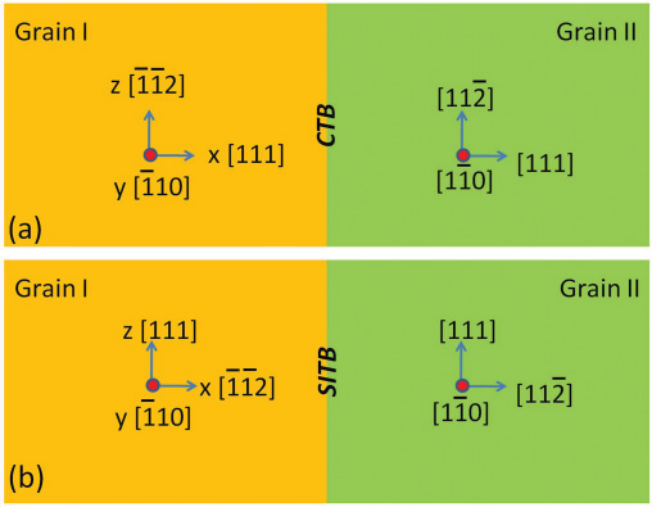

FIG. 1. (Color online) Schematic configurations of Cu bicrystals with a CTB (a) and a SITB (b), and shock loading geometry. Shock loading is along the x-axis.

MD simulations yield trajectories from which some physical properties can be extracted. Given our shock simulation geometry, we divide the simulation cell into fine bins only along the x-direction, and the average physical properties are obtained within each bin (the 1D-binning analysis[26]), such as density, stress tensor (σ_{ij}), particle velocity, and temperature profiles along the x-axis at different stages of compression, release, and tension. The center-of-mass velocity of a bin is removed when calculating temperature and stress. Stress for each bin is the averaged virial stress plus thermal contributions.

We characterize the local deformation and local structure around an atom with a coordination number, the local von Mises shear strain,[48] and centrosymmetry parameter.[49] Coordination number can resolve voids, von Mises shear strain may reveal local shear features within a grain and at a GB, and centrosymmetry parameter can distinguish different atomic packing orders, including the original face-centered-cubic (fcc) packing, hexagonal-close-packed (hcp) stacking faults and twins, and other defects in nonclose-packed structure.

III. RESULTS AND DISCUSSION

The flyer plate-target impact yields shock waves propagating into the target and the flyer plate, which are then reflected at the respective free surfaces as centered simple rarefaction (release) fans, and their interactions induce an evolving tensile region and spall in the target for sufficiently strong shocks, as illustrated in the snapshots [Figs. 2(a)–2(d)] and the conventional position-time (x-t) diagrams [Fig. 2(e) and Fig. 3]. The impact-induced shocks (the elastic shock or elastic precursor and plastic shock), the subsequent interaction between the elastic wave/plastic wave with GB, the release fans originating at the free surfaces, and the interaction of the

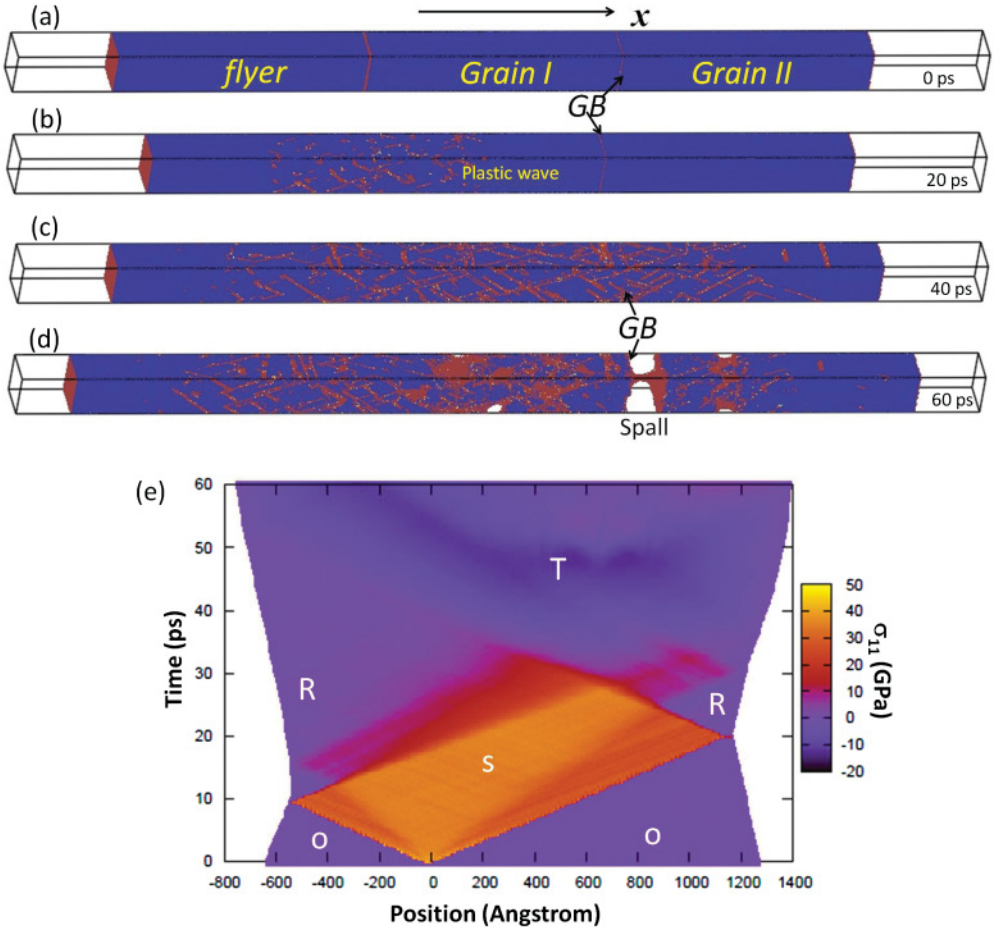

FIG. 2. (Color online) (a)–(d) Snapshots of shock compression, release and spallation in the CTB bicrystal loaded at $u_p = 0.75$ km/s, and (e) the corresponding x-t diagram. The impact plane is at $x = 0$. Color coding in (e) is based on σ_{11}. Region O: unshocked; S: shocked; R: release; T: tension.

opposing release fans lead to well-defined shock, GB plasticity, release, and tension regions in the x-t diagrams. If u_p is sufficiently high, spallation is induced. The wave propagation and interactions related to shock, GB plasticity, release, and tension are illustrated with the evolution of σ_{11} and the von Mises stress ($\sigma_v = \sigma_{11} - \sigma_{22}/2 - \sigma_{33}/2$) for CTB and SITB [Figs. 2(e) and 3].

Structure changes and shear may occur during compression and tension and lead to "plastic" deformation but can be partially reversed during release. Upon spall, the tensile stress is reduced, inducing recompression waves propagating toward the free surfaces. Spall reduces local tension and raises the local temperature. The waves can then be trapped and reverberate between the "spall plane" and target (or flyer plate) free surface. We compare in further discussion the detailed shock response (plasticity and spall) of CTB- and SITB-bicrystals in terms of the elastic shock triggers GB plasticity, GB effects on elastic and plastic shock wave propagation including shock decay (GB damping effect), dynamic GB modification, spall damage, and surface step formation.

A. The interactions of elastic and plastic shock waves with CTB and SITB

Upon collision, both the elastic and plastic shocks in the target propagate toward the GB from the impact plane (Figs. 2 and 3). For CTB the GB region is essentially intact upon the passage of the leading elastic shock [at ~10 ps and 600 A; Fig. 3(a)], while one reflected elastic shock in Grain I and one plastic shock in Grain II are induced at the SITB region [Fig. 3(b)]. The GB plasticity near the SITB is triggered by the elastic precursor initiated on the impact plane at $t \approx 10$ ps before the arrival of the plastic shock wave.

In order to understand the unique shock response of SITB, we first examine the GB structures. As revealed by previous investigations,[41,42] SITB can be represented as a set of Shockley partial dislocations on a {111} plane with a repeatable sequence b_3:b_1:b_2 [Fig. 4(a)]. The Burgers vector b_1 is equal to $1/6[11\bar{2}]$, a pure edge partial dislocation; b_2 and b_3 are equal to $1/6[\bar{2}11]$ and $1/6[1\bar{2}1]$, respectively, both of which are mixed partial dislocations with opposite-sign screw components [Fig. 4(b)]. The sum of the Burgers vectors of these three partials in one triple unit equals zero. In the absence of external stress, the dissociation of partial dislocations can occur spontaneously, and the width of the dissociated region is only a few core sizes [less than ~1 nm; Fig. 4(a)]. Under external stress, the equilibrium width of the dissociated region increases, and the SITB dissociates into two tilt walls bounding a 9R phase (ABCBCACAB). One tilt wall results from the glide of the partial dislocation b_1 away from the SITB, and the other consists of the other two partial dislocations b_2 and

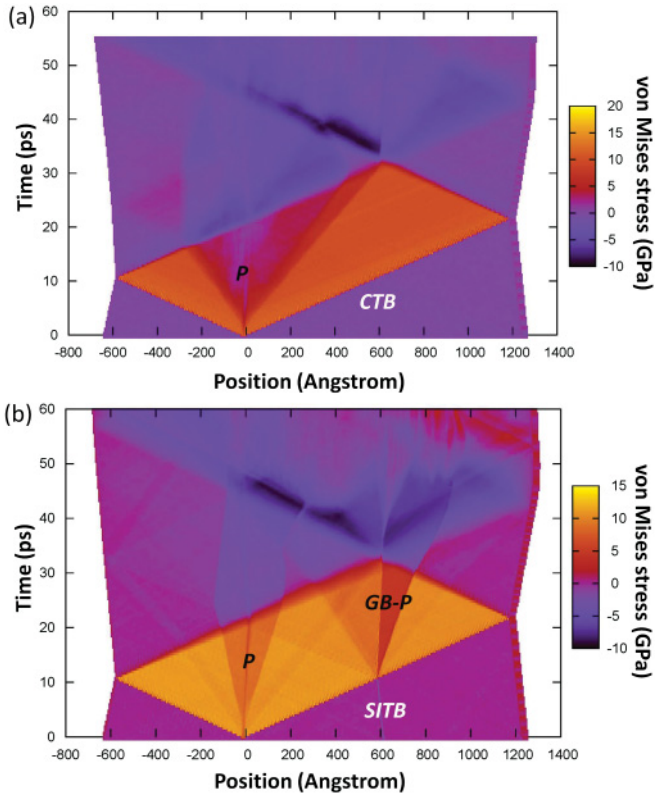

FIG. 3. (Color online) The x-t diagrams for the CTB (a) and SITB (b) bicrytsals shock-loaded at $u_p = 0.375$ km/s. The impact plane is at $x = 0$. Color coding is based on local von Mises stress. Region P: impact plane plastic wave; GB-P: grain boundary plasticity.

b_3 that may remain at their initial positions. The summed Peierls barrier acting on the paired partials b_2 and b_3 is higher than that on b_1, leading to possible anisotropic mechanical response. The observed GB plasticity in Fig. 3(b) is due to the propagation of b_1 partials located at the SITB upon the arrival of elastic shock wave.

We explore $u_p = 0.375$, 0.5, and 0.75 km/s for CTB and SITB subjected to both elastic and plastic shock loading (Figs. 2, 3, 5, and 6). In all the cases, CTB shows similar features as in Figs. 3(a), 5(a), and 5(b). The GB is essentially intact upon the passage of the elastic shock, and the plastic

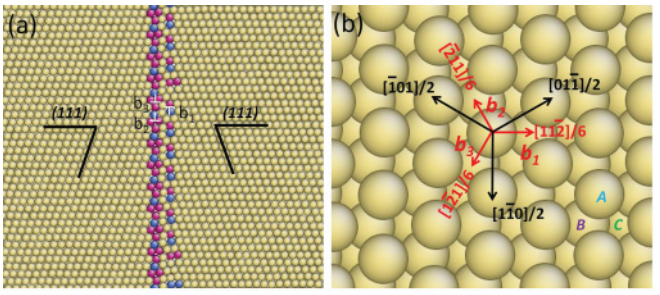

FIG. 4. (Color online) (a) The initial atomic configuration of SITB. SITB contains a set of Shockley partial dislocations on a {111} plane with a repeating sequence of b_3:b_1:b_2; (b) Projection onto a {111} plane showing the ABCABC stacking sequence. The stacking can be altered by the glide of any of the three Shockley partial dislocations.

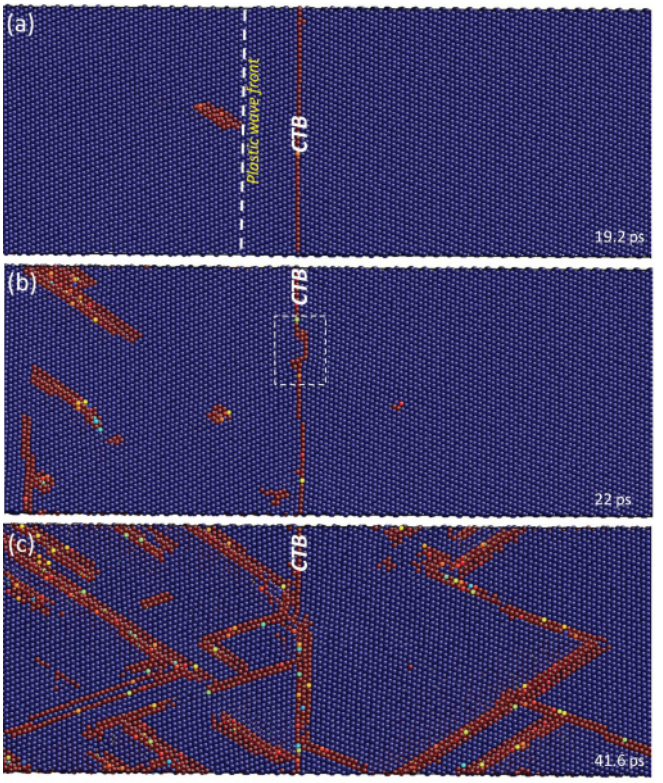

FIG. 5. (Color online) Snapshots of the CTB response to the elastic and plastic shocks ($u_p = 0.375$ km/s): (a) no GB plasticity upon the passage of the elastic precursor; (b) and (c) GB steps produced by the plastic shock (dislocation slip).

shock only induces minor structural changes [e.g., small GB steps, Fig. 5(b)] as the dislocations are transmitted through CTB.[31,32,37] The structural integrity of the CTB is largely preserved during shock compression [during tension as well, Fig. 5(c)].

In contrast, the SITB region displays pronounced GB plasticity, which varies with the impact velocity (Fig. 6). At $u_p = 0.375$ km/s, the elastic shock wave induces GB plasticity only in Grain II via activating b_1 partial dislocations [Fig. 6(a)]. At $u_p = 0.5$ km/s, the GB plasticity due to the elastic precursor is observed in both Grain I and Grain II since the partials located at both sides are activated at this shock strength, and the propagation of partial dislocation b_1 in Grain II is faster than in Grain I [Fig. 6(b)]. At $u_p = 0.75$ km/s, the fast-propagating plastic shock wave originated at the impact plane arrives at the SITB before the GB partial dislocations have a chance to glide away from the SITB into Grain I, thus impeding their development [Fig. 6(c)]. As a result, the GB plasticity occurs only in Grain II but not Grain I. The plastic shock wave interacts with the GB plasticity in Grain II and triggers plasticity along other slip planes [e.g., in Grain II, Fig. 6(c)]. Those results demonstrate the significant effect of GB characteristics on its shock response.

B. Effect of CTB and SITB on shock wave damping

Besides the differences in the structural features, the stress profiles also show corresponding disparities between CTB and SITB. Figure 7 compares the evolution of σ_{22} for CTB and

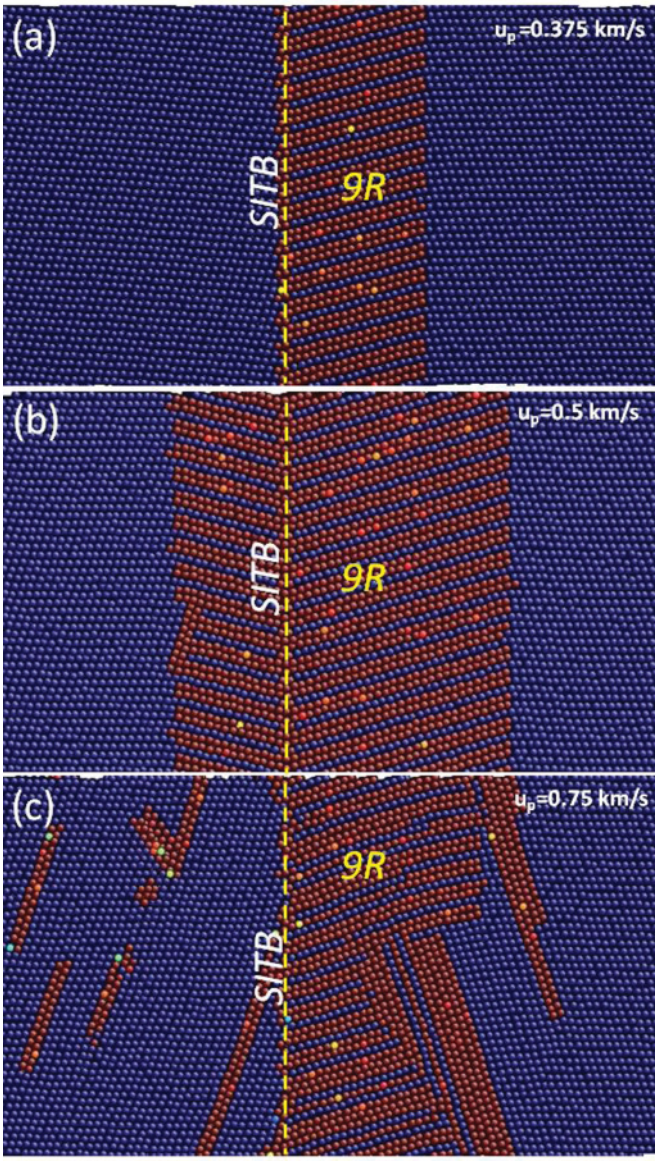

FIG. 6. (Color online) GB-plasticity induced by the elastic shock at SITB for different shock strengths at $t = 16$ ps. The 9R structure denotes the repeating stacking sequence of ABCBCACAB.

SITB shock-loaded at $u_p = 0.75$ km/s. (σ_{22} is the most illustrative among σ_{11}, σ_{22}, and σ_{33} as regards the wave features.) Consistent with the negligible structure changes at CTB (Fig. 5), the GB induces negligible changes in stresses as well [Fig. 7(a)]. However, the elastic precursor induces GB plasticity "spikes" accompanied by a decay in the elastic-wave amplitude when crossing the SITB [8 ps vs 12 ps and 16 ps; Fig. 7(b)], and a small GB-induced plastic-wave plateau develops later (20 ps). The elastic precursor decay is due to the GB plasticity triggered by the elastic shock (Fig. 6). However, the plastic shock wave initiated from the impact plane first interacts with the elastic-precursor-induced plastic wave in Grain I (16 ps), then arrives at SITB and passes through it, and further interacts with the GB plasticity in Grain II (16 ps to 24 ps). Through these interactions, the strength of plastic shock wave appears to be reduced [Fig. 7(b) at 24 ps]. As a result, a four-wave structure is formed across the SITB, including the transmitted elastic shock, GB plastic shock, transmitted plastic shock, and plastic shock, marked in Fig. 7(b) at 24 ps by numbers 1–4. Thus, SITB is capable of modulating elastic and plastic shock waves via partial dislocation gliding and interaction and then induces shock decay. In contrast, CTB remains intact upon shock loading given its rigidity. Those results indicate that the critical influence of GB characteristics on wave propagation in shocked bicrystals.

Shock-damping materials are very important for materials engineering and industrial applications.[50] In general, foams can damp shock wave considerably and is widely used as damping materials,[51,52] but it requires a large volume of foams to damp strong shocks. It would be desirable to explore full-density damping materials. According to the unique feature of SITB shown previously, we may design a new type of damping materials containing many SITBs. We thus investigate the damping efficiency of SITBs with rigid-wall impact simulations of a model Cu-multilayer structure containing 53 SITBs ($\sim$1.5 μm). Shocks propagate from the impact end toward the free surface end of the multilayer structure. The x-t-P diagram for the shocked 53-GB structure [Fig. 8(a)] shows roughly three-wave features, the narrow elastic precursor, and two plastic wave regimes (labeled as E, P_1, and P_2), and the rapid decay of the elastic precursor can be readily identified (color variation). We quantify the elastic shock strength as a function of propagation distance at different time [Fig. 8(b)]: P decreases from an initial value of 10.7 to 2.18 GPa after the elastic precursor traverses 53 SITBs, corresponding to an elastic shock decay of $\sim$80%. The decay processes can be divided into two stages separated at the turning point indicated by the arrow in Fig. 8(b). The turning point approximately corresponds to the transition from the two-side to one-side GB plasticity as triggered by the elastic shock. In the former case (GB plasticity occurs on both sides of a SITB), more energy is dissipated via plasticity than the latter case, thus inducing more pronounced decay. The elastic precursor decay in P is consistent with the plasticity activities. The snapshots in Figs. 8(c) and 8(d) represent the impact end (without considerable decay; early stage) and free-surface end (after considerable decay; later stage), showing profuse plasticity (GB and grain interior) and localized plasticity (only at SITB), respectively. We expect that the elastic shock induce negligible GB plasticity after sufficient propagation, and the plastic shock decay become more pronounced via triggering GB plasticity in a manner similar to the elastic precursor. However, the plastic wave decay cannot be fully explored due to the limitation on the system sizes.

Previously, the elastic precursor decay was attributed to the stress relaxation behind elastic shock front.[53] Alternatively, we found in our MD simulations[54] that the elastic precursor decay can just be the separation dynamics of the elastic shock from the plastic shock, and the decay regime represents the mixed elastic and plastic states. However, the GB-induced plasticity as seen in SITB is another effective decay mechanism.

C. Dynamic modification of the GB region, spallation, and surface step formation

The reflection of shock waves at the target and flyer plate-free surfaces leads to the formation of release fans

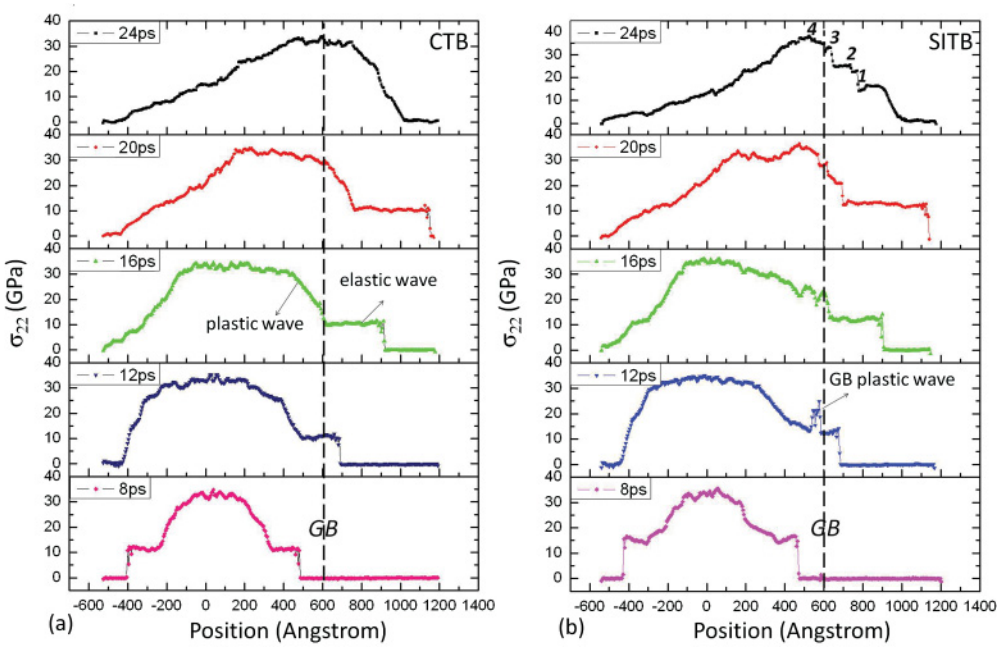

FIG. 7. (Color online) Evolution of the stress wave profiles for CTB (a) and SITB (b) shock-loaded at $u_p = 0.75$ km/s. GB locations are marked with the dashed lines. Also see text.

at the respective free surfaces, and their interaction in the target induces an evolving tensile region and spall damage. During tension, spallation, and later stages, rich dynamic microstructure features are observed, which also strongly depend on the GB characteristics of CTB and SITB.

Figure 9 demonstrates the evolution of the SITB region during shock, release, tension, and spall stages for $u_p = 0.5$ km/s: the preshock state [Fig. 9(a)], elastic shock-induced GB plasticity [Fig. 9(b)], SITB to multifold-twinning transformation at the tension stage [Figs. 9(c)–9(e)], and void formation [Fig. 9(f)]. Due to its high mobility, SITB evolves into a threefold twin region via the slip of partials dislocations at the SITB. Twinning partial first nucleates in Grain I [b_{p1} in Fig. 9(c)], and during its slipping part of the SITB is shifted toward Grain II side. Then another twinning partial nucleates in Grain II [b_{p2} in Fig. 9(d)]. Through the collective slip activities of these two partial dislocations, part of the SITB is dissolved into a region separated by two twin boundaries [Fig. 9(e)]. After this transformation, the whole region can be regarded as a threefold twin. Such SITB transformation

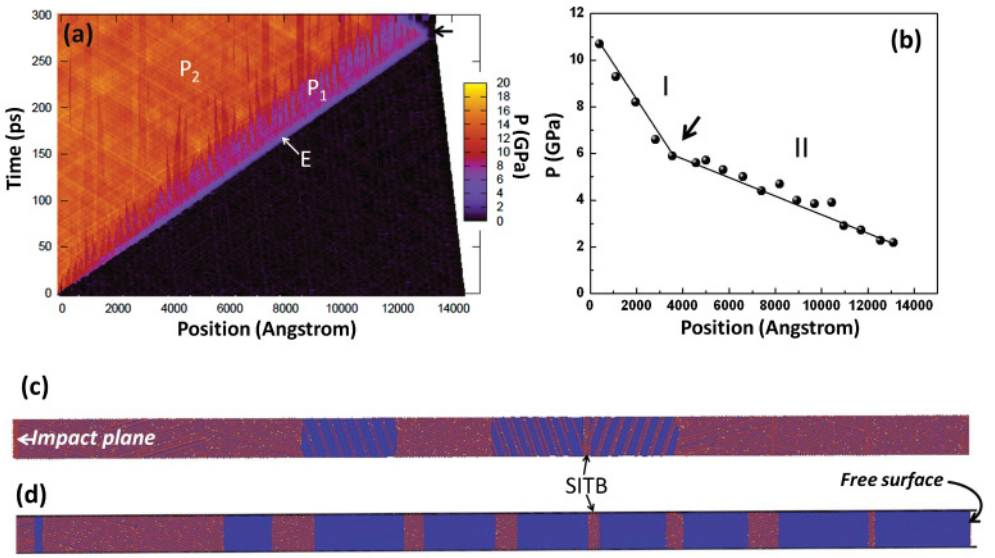

FIG. 8. (Color online) (a) The x-t diagram for shock loading of the Cu multilayers contain 53 SITBs at $u_p = 0.375$ km/s. Color coding is based on pressure ($P = (\sigma_{11} + \sigma_{22} + \sigma_{33})/3$), and the arrow indicates the reflection of the elastic shock wave front at the free surface. E and P (P_1 and P_2) stand for elastic wave and plastic wave, respectively. (b) The elastic precursor decay due to GB plasticity. The position refers to the elastic shock front position during its propagation. Atomic configurations at $t = 270$ ps near the impact end (c) and the free surface end (d).

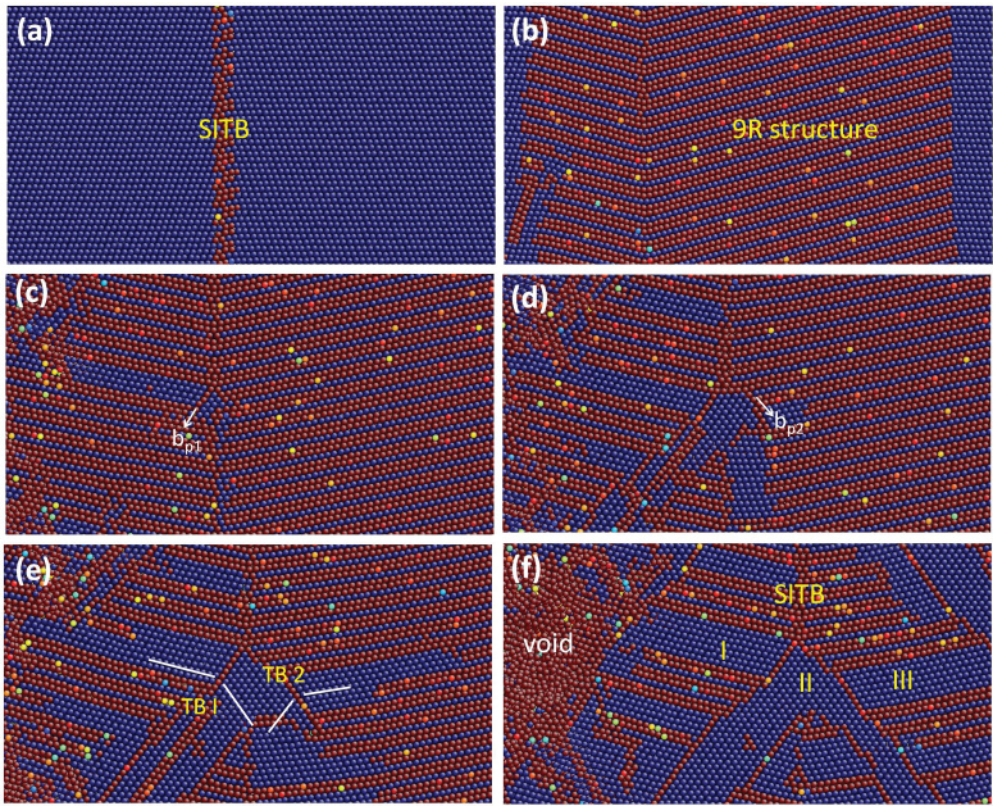

FIG. 9. (Color online) Structural variation of SITB during shock, tension and spallation for $u_p = 0.5$ km/s: (a) before the elastic shock arrival; (b) GB plasticity during elastic and plastic shock compression; (c) the first partial dislocation (b_{p1}) nucleation at SITB which slips in Gain I during tension; (d) the second partial dislocation (b_{p2}) formation in SITB which slips in Grain II; (e) partial transformation of the SITB into a threefold twin during tension; (f) void nucleation in Grain I, away from the original SITB.

is observed for $u_p = 0.375$ km/s as well. Multifold deformation twins were observed both in experiments and MD simulations of nanocrystalline metals and alloys,[55–58] and a sequential twinning mechanism was proposed to provide a pathway for the formation of multifold-deformation twins. However, such a mechanism requires an orientation change of the applied stresses. Cao *et al.*[56] suggested the mechanism for formation of multifold-deformation twins under uniaxial tension loading through introducing pre-twins. However, the threefold-deformation twin in the present case is formed at the SITB during tension due to the special features of SITB. For the particular SITB geometry, there are two slip planes at $\sim 19.5^\circ$ with SITB, which can be readily activated during tension and act as the sequential twinning partial-slip planes [Fig. 9(c)]. Those results further show that the high mobility of SITB may give rise to special mechanical properties and shock responses. In contrast, the structures of CTB at tension stage show various dislocation-CTB interactions as during the shock compression stage, but neither pronounced CTB variations nor partial GB dissolution is observed (Fig. 5).

The shocks are reflected at the free surfaces as release fans, which unload the shocked materials to zero stresses and lower temperature and further into tension and cause spall damage.[9,28,29,59] Due to the striking difference in the characteristics of CTB and SITB, their response to spall damage is distinctively different. Under tension, tensile plasticity, and remnant compression plasticity, defects, solid state disordering, and their interactions induce local weakening, and consequently, nanovoids nucleate at GBs or the weakened region of grain interiors. We characterize voids with coordination number since the surface atoms enclosing a void are undercoordinated. Nanvoids are revealed by such atoms with coordination number smaller than eight in selected configurations under tension. Nanovoids can be of different size and shape during void growth and coalescence (Fig. 10).

At $u_p = 0.375$ km/s, there is no void formation for both CTB and SITB bicrystals, while at $u_p = 0.75$ km/s, voids are nucleated widely in both the CTB and SITB bicrystals due to the high shock strength. Thus, the intermediate shock strength ($u_p = 0.5$ km/s) is more appropriate for the comparison. For CTB, nanovoids are observed both within the grain interior and at CTB [Fig. 10(a)]. However, the major damage occurs at CTB, which leads to fracture [Fig. 2(c) and Fig. 10(a)]. Due to the strong impeding effect of CTB on dislocation slip, stress concentration tends at GB and makes CTB a preferred site for void nucleation.[31,60] In contrast, voids nucleate within the grain interior but not at the GB for the SITB bicrystal [Fig. 10(b)]. The void nucleation site coincides with the region where the plastic shock wave encounters backward-propagating GB plastic wave in Grain I of the SITB bicrystal [Fig. 6(b)]. Such wave interaction leads to highly sheared region and disordering, and this "predamaged" region is a preferred void nucleation site [Figs. 9(f) and 10(b)]. Our simulations show that void nucleation tends to occur at CTB but not necessarily

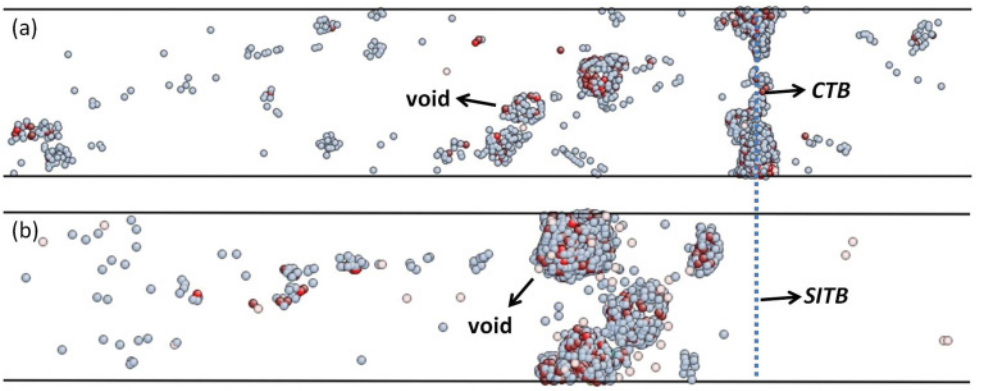

FIG. 10. (Color online) Difference in void nucleation for CTB (a) and SITB (b) shock loaded at $u_p = 0.5$ km/s.

at SITB. The dislocation and twinning activities around SITB "shift" the damage to the grain interior. In this regard SITB itself could be more resistant to spall damage than CTB, which is unexpected for quasistatic loading.

Surface-step formation during plastic deformation is quite common and can be induced by various mechanisms, such as slip localization, twinning, or kinking.[61–64] The mechanisms and processes leading to surface step during quasistatic loading can be readily identified or monitored *in situ* with optical microscope or scanning electron microscope.[61–64] However, for shock loading, the mechanism and process of surface intrusion and extrusion still remain unclear, largely due to the ultrafast nature of dynamic loading.[9]

In the present simulations we reveal a dynamic twinning mechanism for step formation on the surface of the spalled layer. The snapshot in Fig. 11(a) shows a pronounced surface

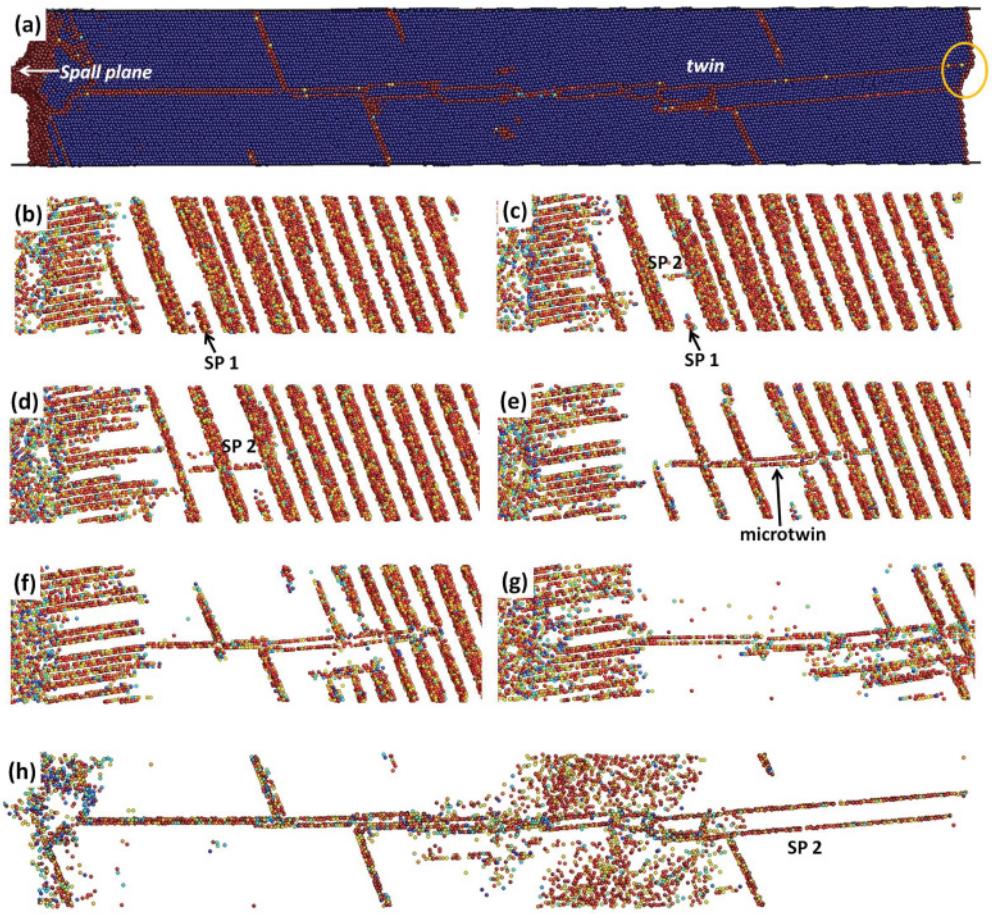

FIG. 11. (Color online) Formation sequence of a twinning-induced surface step for SITB shock-loaded at $u_p = 0.75$ km/s. (a) A bamboo-like deformation twin produces a surface step at the free surface of Grain II at $t = 60$ ps. (b) to (h) Detailed deformation twin formation process at $t = 33.6$, 34, 36, 38.8, 40, 42.8, and 60 ps, respectively; its thickening and propagation lead to the surface step. SP denotes slip plane.

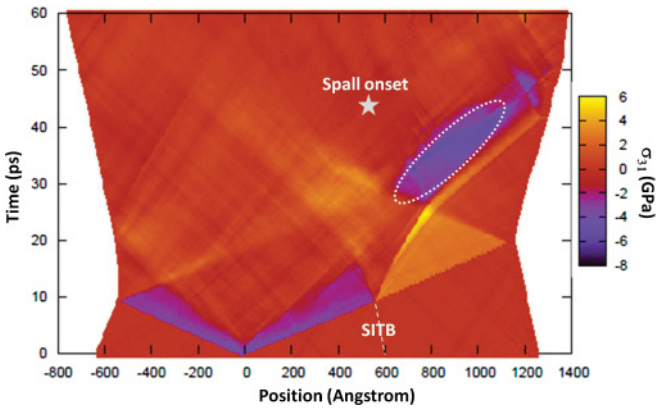

FIG. 12. (Color online) The x-t diagrams for shock loading of the Cu bicrystal with SITB at $u_p = 0.75$ km/s. Color coding is based on σ_{31}. The region marked by the ellipse shows the strong shear stress region in Grain II during tension and spallation stage.

step with the circled area on the target-free surface for the SITB bicrystal shock-loaded at $u_p = 0.75$ km/s, which is induced by the bamboo-like deformation twins (8-atom-layers thick at the end). The process of deformation twin nucleation and surface-step formation is displayed in Figs. 11(b) to 11(h), as driven by the dynamic stress states (tension and shear are dominant; Fig. 12). The x-t diagram in Fig. 12 shows pronounced shear stress σ_{31} due to the wave interaction in the relevant time-space regime (circled). While the tension partially recovers the compression-induced deformation [slanted $\{111\}$ slip planes labeled as SP1; Figs. 11(b)–11(h)] due to the strain path reversal, the shear stress σ_{31} (and tension) leads to nucleation and growth of a small stacking fault [the "horizontal" $\{111\}$ slip planes labeled as SP2, Figs. 11(c) and 11(d)]. The interaction of this stacking fault and the preexisting, retreating slip planes SP1 facilitates cross-slip and transforms the stacking fault into a microtwin [Fig. 11(e)]. As this process continues, the twin thickens and grows toward the free surface, and forms a bamboo-like structure. The angle between the twinning plane and the xy-plane increases as the twin grows, giving rise to the surface step when the twin reaches the free surface. The compression-induced plasticity is almost fully recovered during this process [Fig. 11(h)]. The size of the simulation cell and the periodic boundary conditions should also have some effect on the twinning process and the size of the step formed at the back surface. However, our simulations indicate that deformation twinning is a possible mechanism to produce surface steps during tension and spallation stage rather than shock compression.

For the SITB bicrystal shock-loaded at $u_p = 0.375$, 0.5, 0.75, and 1 km/s, the surface step is only observed for $u_p = 0.75$ km/s. The nucleation of the deformation twin requires a critical shear stress (the circled regime in Fig. 12).[65] The maximum shear stress σ_{31} is ~8 GPa for $u_p = 0.75$ km/s, but it is much lower ($\leqslant$4 GPa) for $u_p = 0.375$ and 0.5 km/s. This indicates the critical nucleation shear stress for the deformation twin is higher than 4 GPa but smaller than 8 GPa in this case. For $u_p = 1$ km/s, the maximum shear stress σ_{31} is ~10 GPa and the deformation twin could nucleate. However, the growth of the deformation twin is impeded by the widely spread spall damage for such high a shock load, so no surface step is formed. For CTB, no surface step is observed at all impact velocities. Thus, the surface step formation during shock loading only occurs at some particular cases, and strongly depends on microstructure (orientation and GB characteristics) and dynamic loading conditions.

Our comparative study on the response of CTB and SITB to elastic and plastic shock waves, and subsequent tension demonstrates the importance role of GB structures in the corresponding dynamic mechanical properties. While CTB retains high integrity to both elastic and plastic shocks but is the preferred site for spall damage, SITB shows rich dynamic structural modifications and modulates wave propagation accordingly, and may shift the damage off the GB. These investigations reveal the unique features of CTB and SITB upon the dynamic loading, which could be exploited for interface engineering in future.

IV. CONCLUSION

Comparative MD simulations of Cu bicrystals with $\Sigma 3$ CTB and SITB under shock wave loading reveal drastically different shock responses (deformation and spallation) of different twin GBs. At the shock compression stage, elastic shock wave can readily trigger GB plasticity at SITB but not at CTB. The SITB can induce considerable wave attenuation such as the elastic precursor decay via activating GB dislocation slip. At the tension stage, spallation tends to occur at CTB but not at SITB due to the high mobility of SITB. The SITB region transforms into a threefold twin via a sequential partial dislocation slip mechanism, while CTB preserves its integrity before spallation. The surface step formation for the SITB bicrystal is observed for certain loading conditions due to deformation twinning during tension. Our results underscore the important roles of GBs and loading in dynamic response of bicrystal and likely polycrystalline metals.

ACKNOWLEDGMENTS

This work was supported by ASC/LDRD programs at LANL and the PSAAP project at Caltech. LANL is operated by Los Alamos National Security, LLC for the US Department of Energy under Contract No. DE-AC52-06NA25396.

*wzhanmail@gmail.com
†sluo@lanl.gov

[1] A. P. Sutton and R. W. Balluffi, *Interfaces in Crystalline Materials*, (Clarendon Press, Oxford, 1995).
[2] T. G. Langdon, Acta Metall. Mater. **42**, 2437 (1994).
[3] M. Winning, G. Gottstein, and L. S. Shvindlerman, Acta Mater. **49**, 211 (2001).
[4] V. Randle, Acta Mater. **52**, 4067 (2004).

[5]Z. F. Zhang and Z. G. Wang, Prog. Mater. Sci. **53**, 1025 (2008).
[6]X. Y. Li, Y. J. Wei, W. Yang, and H. J. Gao, Proc. Nat. Acad. Sci. **106**, 16108 (2009).
[7]W. Z. Han, H. J. Yang, X. H. An, R. Q. Yang, S. X. Li, S. D. Wu, and Z. F. Zhang, Acta Mater. **57**, 1132 (2009).
[8]M. A. Meyers and C. T. Aimone, Prog. Mater. Sci. **28**, 431 (1983).
[9]M. A. Meyers, *Dynamic Behavior of Materials* (Wiley, New York, 1994).
[10]M. A. Meyers, A. Mishra, and D. J. Benson, Prog. Mater. Sci. **51**, 427 (2006).
[11]J. C. Sanchez, L. E. Murr, and K. P. Staudhammer, Acta Mater. **45**, 3223 (1997).
[12]D. R. Chichili, K. T. Ramesh, and K. J. Hemker, Acta Mater. **46**, 1025 (1998).
[13]A. Mishra, M. Matin, N. N. Thadhani, B. K. Kad, E. A. Kenik, and M. A. Meyers, Acta Mater. **56**, 2770 (2008).
[14]F. Cao, I. J. Beyerlein, F. L. Addessio, B. H. Sencer, C. P. Trujillo, E. K. Cerreta, and G. T. Gray III, Acta Mater. **58**, 549 (2010).
[15]P. Peralta, S. DiGiacomo, S. Hashemian, S. N. Luo, D. Paisley, R. Dickerson, E. Loomis, D. Byler, and K. J. McClellan, Int. J. Damage Mech. **18**, 393413 (2009).
[16]J. C. F. Millett, S. M. Stirk, N. K. Bourne, and G. T. Gray III, Acta Mater. **58**, 5675 (2010).
[17]L. Wayne, K. Krishnan, S. DiGiacomo, N. Kowali, P. Peralta, S. N. Luo, S. Greenfield, D. Byler, D. Paisley, K. J. McClellan, A. Koskelo, and R. Dickerson, Scr. Mater. **63**, 1065 (2010)
[18]W. Z. Han, A. Misra, N. A. Mara, T. C. Germann, J. K. Baldwin, T. Shimada, and S. N. Luo, Philos. Mag. **91**, 4172 (2011).
[19]T. C. Germann, B. L. Holian, P. S. Lomdahl, and R. Ravelo, Phys. Rev. Lett. **85**, 5351 (2000).
[20]K. Kadau, T. C. Germann, P. S. Lomdahl, and B. L. Holian, Science **296**, 1681 (2002).
[21]E. M. Bringa, A. Caro, Y. Wang, M. Victoria, J. M. McNaney, B. A. Remington, R. F. Smith, B. R. Torrala, and H. Van Swygenhoven, Science **309**, 1883 (2005).
[22]V. Dremov, A. Petrovtsev, P. Sapozhnikov, M. Smirnova, D. L. Preston, and M. A. Zocher, Phys. Rev. B **74**, 144110 (2006).
[23]S. G. Srinivasan, M. I. Baskes, and G. J. Wagner, J. Appl. Phys. **101**, 043504 (2007).
[24]V. V. Stegailov and A. V. Yanilkin, J. Exp. Theor. Phys. **104**, 928 (2007).
[25]G. E. Norman, Y. Kuksin, V. V. Stegailov, and A. V. Yanilkin, AIP Conf. Proc. **329**, CP955 (2008).
[26]S. N. Luo, Q. An, T. C. Germann, and L. B. Han, J. Appl. Phys. **106**, 013502 (2009).
[27]B. Arman, S. N. Luo, T. C. Germann, and T. Cagin, Phys. Rev. B **81**, 144201 (2010).
[28]S. N. Luo, T. C. Germann, T. G. Desai, D. L. Tonks, and Q. An, J. Appl. Phys. **107**, 123507 (2010).
[29]S. N. Luo, T. C. Germann, D. L. Tonks, and Q. An, J. Appl. Phys. **108**, 093526 (2010).
[30]S. Mahajan, C. S. Pande, M. A. Imam, and B. B. Rath, Acta Mater. **45**, 2633 (1997).
[31]L. Lu, Y. F. Shen, X. Chen, L. H. Qian, and K. Lu, Science **304**, 422 (2004).
[32]L. Lu, X. Chen, X. Huang, and K. Lu, Science **323**, 607 (2009).
[33]X. Zhang, A. Misra, H. Wang, M. Nastasi, J. D. Embury, T. E. Mitchell, R. G. Hoagland, and J. P. Hirth, Appl. Phys. Lett. **85**, 1096 (2004).
[34]X. Zhang, H. Wang, X. H. Chen, L. Lu, K. Lu, R. G. Hoagland, and A. Misra, Appl. Phys. Lett. **88**, 173116 (2006).
[35]E. Ma, Y. M. Wang, Q. H. Lu, M. L. Sui, L. Lu, and K. Lu, Appl. Phys. Lett. **85**, 4932 (2004).
[36]T. Zhu, J. Li, A. Samanta, H. G. Kim, and S. Suresh, Proc. Nat. Acad. Sci. **104**, 3031 (2007).
[37]Z. H. Jin, P. Gumbsch, K. Albe, E. Ma, K. Lu, H. Gleiter, and H. Hahn, Acta Mater. **56**, 1126 (2008).
[38]Y. Kulkarni and R. J. Asaro, Acta Mater. **57**, 4835 (2009).
[39]A. Singh, L. Tang, M. Dao, L. Lu, and S. Suresh, Acta Mater. **59**, 2437 (2011).
[40]C. J. Shute, B. D. Myers, S. Xie, S. Y. Li, T. W. Barbee, A. M. Hodge, and J. R. Weertman, Acta Mater. **59**, 4569 (2011).
[41]J. Wang, O. Anderoglu, J. P. Hirth, A. Misra, and X. Zhang, Appl. Phys. Lett. **95**, 021908 (2009).
[42]J. Wang, N. Li, O. Anderoglu, X. Zhang, A. Misra, J. Y. Huang, and J. P. Hirth, Acta Mater. **58**, 2262 (2010).
[43]J. P. Hirth and J. Lothe, *Theory of Dislocations (Krieger, Melbourne*, FL, 1992).
[44]M. A. Tschopp and D. L. Mcdowell, Philos. Mag. **87**, 3147 (2007).
[45]Y. Mishin, M. J. Mehl, D. A. Papaconstantopoulos, A. F. Voter, and J. D. Kress, Phys. Rev. B **63**, 224106 (2001).
[46]J. Stadler, R. Mikulla, and H. R. Trebin, Int. J. Mod. Phys. C **8**, 1131 (1997).
[47]S. J. Plimpton, J. Comp. Phys. **117**, 1 (1995).
[48]F. Shimizu, S. Ogata, and J. Li, Mater. Trans. **48**, 2923 (2007).
[49]J. Li, Model. Simul. Mater. Sci. Eng. **11**, 173 (2003).
[50]G. Ben-Dor, O. Igra, and T. Elperin, *Handbook on Shock Waves* (Academic Press, Boston, Massachusetts, 2000).
[51]B. I. Palamarchuk and A. T. Malakhov, Comb. Explo. and Shock Waves **26**, 753 (1990).
[52]A. Britan, B.-G. Dor, H. Shapiro, and M. Liverts, Shreiber. Coll. & Surf. A-Physicochem. and Eng. Aspects **309**, 137 (2007).
[53]J. R. Asay, G. R. Fowles, and Y. M. Gupta, J. Appl. Phys. **43**, 744 (1972).
[54]S. N. Luo (unpublished).
[55]Y. T. Zhu, X. Z. Liao, and R. Z. Valiev, Appl. Phys. Lett. **86**, 103112 (2005).
[56]A. J. Cao and R. G. Wei, Appl. Phys. Lett. **89**, 041919 (2006).
[57]Y. T. Zhu, J. Narayan, J. P. Hirth, S. Mahajan, X. L. Wu, and X. Z. Liao, Acta Mater. **57**, 3763 (2009).
[58]X. H. An, Q. Y. Lin, S. D. Wu, Z. F. Zhang, R. B. Figueiredo, N. Gao, and T. G. Langdon, Scr. Mater. **64**, 249 (2011).
[59]Y. Ashkenazy and R. S. Averback, Appl. Phys. Lett. **86**, 051907 (2005).
[60]S. Qu, P. Zhang, S. D. Wu, Q. S. Zang, and Z. F. Zhang, Scr. Mater. **59**, 1131 (2008).
[61]Z. S. Basinski and S. J. Basinski, Acta Metall. **33**, 1307 (1985).
[62]T. E. Mitchell, P. Peralta, and J. P. Hirth, Acta Mater. **47**, 3687 (1999).
[63]W. Z. Han, Z. F. Zhang, S. D. Wu, S. X. Li, and Y. D. Wang, Philos. Mag. Lett. **86**, 435 (2006).
[64]Q. Yu, Z. W. Shan, J. Li, X. X. Huang, L. Xiao, J. Sun, and E. Ma, Nature **463**, 335 (2010).
[65]W. Z. Han, Z. F. Zhang, S. D. Wu, and S. X. Li, Philos. Mag. **88**, 3011 (2008).